Letter

Non-Abelian braiding of Weyl nodes via symmetry-constrained phase transitions

Siyu Chen [1,*] Adrien Bouhon [2,†] Robert-Jan Slager [1,‡] and Bartomeu Monserrat [1,3,§]

[1] *TCM Group, Cavendish Laboratory, University of Cambridge, J. J. Thomson Avenue, Cambridge CB3 0HE, United Kingdom*

[2] *Nordic Institute for Theoretical Physics (Nordita), Stockholm University and KTH Royal Institute of Technology, Hannes Alfvéns väg 12, Stockholm SE-106 91, Sweden*

[3] *Department of Materials Science and Metallurgy, University of Cambridge, 27 Charles Babbage Road, Cambridge CB3 0FS, United Kingdom*

(Received 2 September 2021; accepted 14 February 2022; published 28 February 2022)

Weyl semimetals are arguably the most paradigmatic form of a gapless topological phase. While the stability of Weyl nodes, as quantified by their topological charge, has been extensively investigated, recent interest has shifted to the manipulation of the location of these Weyl nodes for non-Abelian braiding. To accomplish this braiding it is necessary to drive significant Weyl node motion using realistic experimental parameter changes. We show that a family of phase transitions characterized by certain symmetry constraints impose that the Weyl nodes have to reorganize by a large amount, shifting from one high-symmetry plane to another. Additionally, for a subset of pairs of nodes with nontrivial Euler class topology, this reorganization can only occur through a braiding process with adjacent nodes. As a result, the Weyl nodes are forced to move a large distance across the Brillouin zone and to braid, all driven by small temperature changes, a process we illustrate with $Cd_2Re_2O_7$.

DOI: 10.1103/PhysRevB.105.L081117

Introduction. The discovery of topological insulators [1,2] has reinvigorated an interest in band theory over the past decade. The initial ideas behind topological insulators have been extended to include different crystalline symmetries, resulting in a plethora of topological characterizations [3–23], and also to topological semimetals and superconductors [24–26]. Within these, Weyl semimetals represent an ultimate consequence of translational symmetry, allowing for locally stable band crossings that carry a topological charge. More recently, there has also been an interest in braiding Weyl nodes residing in different band gaps in systems exhibiting reality conditions, as this process can result in configurations in which nodes in the same gap have similar charges. The resulting obstruction for the nodes to annihilate is characterized by a new type of multigap invariant known as the Euler class [23,27–37].

The practical use of Weyl nodes requires their manipulation with external parameters, and there is a growing body of literature in this direction [38]. Examples include the use of stress and strain [39,40], coupling to electromagnetism and light [41,42], and disorder [43–46]. However, in these proposals the Weyl nodes only move by a small fraction of the Brillouin zone dimension with experimentally realistic parameter changes, making the manipulation of Weyl nodes impractical. Here, we explore a route to moving Weyl nodes that combines insights from materials science via temperature-driven structural changes with more fundamental theoretical insights that find their origin in symmetry. Namely, we show that in a particular class of structural phase transitions, Weyl nodes need to travel a long distance across the Brillouin zone to follow the relevant symmetry changes, and these large displacements are driven by small temperature changes. We first exemplify this concept using $Cd_2Re_2O_7$ as a material example, and we then provide a more fundamental perspective setting the stage for a general mechanism. This allows us to predict this behavior for a whole class of compounds and symmetries.

Structural phase transitions. $Cd_2Re_2O_7$ is an intriguing material as it is the only known superconductor in the pyrochlore family [47,48]. Interest in its superconductivity has led to extensive exploration of its phase diagram under different conditions [49]. As summarized in Fig. 1(a), $Cd_2Re_2O_7$ crystallizes in a structure of cubic symmetry (phase I, $Fd\bar{3}m$) [50] at ambient temperature and pressure. The structure can be described as two interwoven pyrochlore lattices assembled from Re_4 and Cd_4 tetrahedra, respectively, where the centers of O_6 octahedra coincide with the centers of Re_4 tetrahedra. With gradual cooling, two low-temperature phases with higher conductance appear successively at $T_{s1} =\sim 200$ K [51,52] and $T_{s2} =\sim 120$ K [53,54], both exhibiting tetragonal symmetry but lacking a center of inversion (phase II, $I\bar{4}m2$ and phase III, $I4_122$). Very recently, a magnetic torque experiment has revealed that the transition between phases II and III is mediated by an additional phase of point group D_{4h} or D_2 [55]. Given that this additional phase was not detected in previous experiments with the exact same setting but a relatively large temperature step of 2.5 K [56], the new phase should only exist in a narrow temperature range around T_{s2} of at most 2.5 K.

The noncentrosymmetric lattice, strong spin-orbit coupling, and metallic properties of the two well-characterized low-temperature phases of $Cd_2Re_2O_7$ naturally satisfy the

*sc2090@cam.ac.uk
†adrien.bouhon@su.se
‡rjs269@cam.ac.uk
§bm418@cam.ac.uk

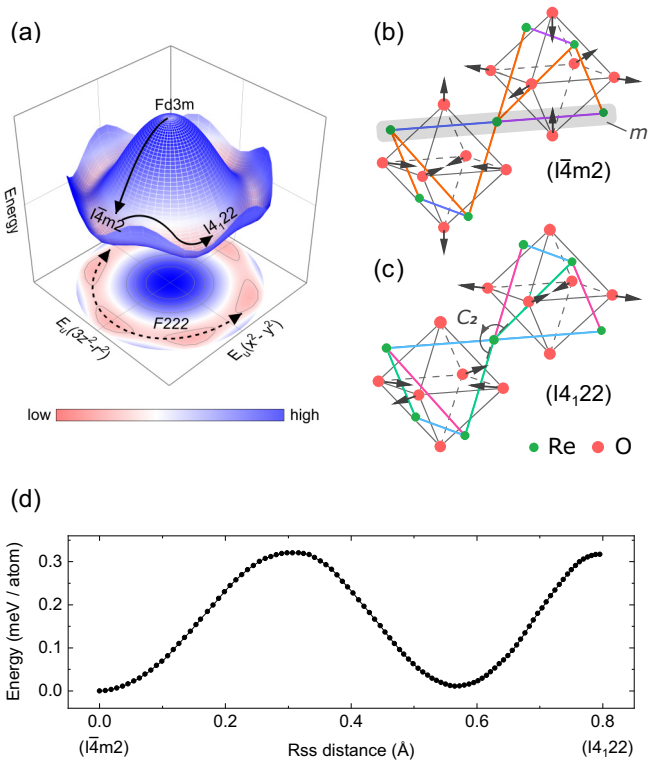

FIG. 1. (a) Energy landscape of $Cd_2Re_2O_7$. The space groups of the three phases observed in experiments are shown on the energy surface. The solid arrows indicate the path of the phase transition during cooling and the dashed arrow indicates the Goldstone mode fluctuating between phases II and III. (b), (c) Distortions of neighboring Re_4 tetrahedra and O_6 octahedra in (b) phase II and (c) phase III. The Re and O ions are represented by the green and red vertices, respectively. The displacement of each O ion is indicated by the arrow attached to the ion. The subtle differences between the edge length of Re_4 tetrahedra responding to O ion movement are distinguished by the colors. The shaded area shows the dihedral mirror plane falling along the "indigo" and "purple" edge of Re_4 tetrahedra and the curved arrow shows the twofold axis through the connecting Re ion. (d) Saddle points on the energy surface from phase II to III as a function of the root sum squared distance of atoms, where the energy of phase II has set to zero.

prerequisites for nonmagnetic Weyl semimetals, providing an ideal platform to study the movement of Weyl nodes constrained by crystallographic symmetry changes. This inspires us to consider a smooth path connecting phases II and III. The crystal structures of phases II and III are obtained through a first-principles phonon calculation performed relativistically (including spin-orbital coupling) with a revised Perdew-Burke-Ernzerhof generalized gradient approximation functional for solids (PBEsol) [57] on phase I reported in the Inorganic Crystal Structure Database [58] (see calculation details in Supplemental Material (SM) [59] and also Refs. [60–63] therein), and the intermediate structures are obtained using the nudged elastic band (NEB) algorithm [64] to optimize a number of linear interpolated structures between phases II and III. The results show that all fully optimized intermediate structures belong to the same space group, constituting a smooth transition path of $F222$ symmetry. Including the start and end of the path (namely, phases II and III), any crystal structure on the path can be interpreted as a consequence of structural distortions of phase I, which is dominated by Cd and O ion displacements. Figures 1(b) and 1(c) visualize the distortions of O ions occurring in phases II and III. It is worth noting that two neighboring O_6 octahedra have displacements with opposite directions, thus the inversion symmetry of the system is broken. Interestingly, although the distortion does not have a Jahn-Teller origin but instead is very likely driven by strong spin-orbital coupling [65], it exhibits extremely similar behavior compared to the Jahn-Teller effect occurring among d-orbital coordination complexes in which E_g electronic states are coupled to E_g vibrational modes. In phase II, the distortion conserves the symmetry of the horizontal square of the O_6 octahedra and gives half of the O_6 octahedra an elongation along the vertical direction whereas the other half a compression. In phase III, the horizontal square is distorted to a rhombus, which breaks the vertical mirror planes that fall along the "indigo" and "purple" edges of Re_4 tetrahedra shown in Fig. 1(b). It is also worth noting that in phase II the two neighboring Re_4 tetrahedra are noncongruent; however, when it comes to phase III, they become congruent via losing the mirror plane in phase II and adding a twofold axis through the connecting Re ion, as shown in Fig. 1(c). Such a change in symmetry results in the conversion of the point group of the system from D_{2d} to D_4. We show later that this transition from a fourfold rotoinversion symmetry ($S_{4z} = IC_{4z}^{-1}$ in D_{2d}) to a proper fourfold rotation symmetry (C_{4z} in D_4) drives a major topological transformation of the band structure in reciprocal space.

As a final remark, we emphasize that the path proposed in this work is not just a fictitious computational construct. Its existence is strongly supported by group theory analysis [66] and by the latest magnetic torque experiment performed with extremely small temperature steps [55]. The phenomenological order parameter characterizing the cubic-to-tetragonal phase transitions of $Cd_2Re_2O_7$ corresponds to a twofold degenerate E_u representation of the cubic point group, so it makes sense that the NEB calculation has found a series of orthorhombic intermediate phases of space group $F222$ (the maximal common subgroup of phases II and III) which are induced by a mixture of the two components of the representation. The result from the NEB calculation shows that the energy difference of intermediate phases on the path is anomalously small [$\Delta E \leqslant 0.3\,\mathrm{meV/atom}$; see Fig 1(d)], which is of the order of $\Delta T = 0.4\,\mathrm{K}$ for a structure traversing the whole path. This extremely flat path leads to a quasicontinuous $U(1)$ symmetry of the energy landscape of $Cd_2Re_2O_7$. Breaking this symmetry was predicted to yield a Goldstone mode manifesting as a structural fluctuation between phase II and phase III with vanishing frequency and excitation energy, and this has been observed by polarized Raman scattering and x-ray diffraction experiments [67,68]. In particular, we have found an energy local minimum on the path which has the same energy as phase II, and we propose it as a candidate structure for the newly discovered intermediate phase in Ref. [55].

Mechanism of Weyl node movement. Since the path connecting phases II and III preserves the symmetry of space group $F222$, the key symmetry elements constraining the

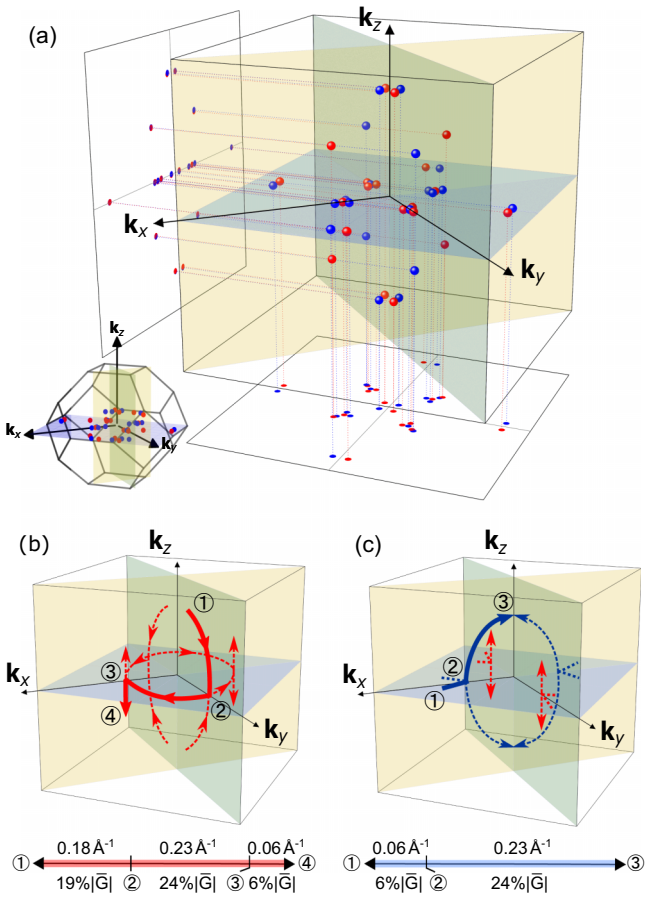

FIG. 2. (a) Weyl nodes in the Brillouin zone of phase II. The chirality of the Weyl nodes is distinguished by the red and blue colors of the balls/dots. The three C_2T-invariant planes are highlighted. The Brillouin zone polyhedron is shown in the lower left corner for reference. (b), (c) The movement of the red and the blue Weyl nodes as the phase transition smoothly progresses from phase II to phase III. The thick arrows indicate the movement of the Weyl nodes of interest, and the dashed arrows indicate the movement of their symmetry-related partners. The bars below show the distances that the Weyl nodes travel on the C_2T-invariant planes, where $|\tilde{G}|$ denotes the cubic root of the volume of the Brillouin zone. See text for more details.

phase transition are three twofold rotation axes along the k_x, k_y, and k_z directions, respectively: C_{2x}, C_{2y}, and C_{2z}. Time-reversal symmetry T is also preserved along the transition path as no magnetic ordering has been observed in experiments [69] or in our first-principles calculations. Hence, there are three mutually perpendicular C_2T-invariant planes dividing the Brillouin zone polyhedron into eight equivalent regions, on which state $|\psi_k\rangle$ can be mapped to itself by a combination of symmetry operators $C_{2i}T$ ($i = x$ or y or z). Figure 2(a) shows the distribution of the Weyl nodes of phase II formed by the two partially occupied bands closest to the Fermi energy E_F, whose main contributions are Re t_{2g} orbitals. There are a total of 20 pairs of Weyl nodes in the whole Brillouin zone located within the energy window of $E_F \pm 100$ meV. Considering the symmetry of the system, there are four independent octets and two independent quartets of Weyl nodes. All of them are pinned exactly on the C_2T-invariant planes, which is in line with the previous theoretical prediction that C_2T symmetry is able to stabilize Weyl nodes [6,23,70]. Additionally, due to the presence of two dihedral mirror planes ($k_x = k_y$ and $k_x = -k_y$ planes) the Weyl nodes flip chirality when mapped from one vertical C_2T-invariant plane to another, thus forming quartets of Weyl nodes at fixed k_z with alternating chirality. $C_{2z}T$ symmetry then maps each quartet of Weyl nodes at k_z to a quartet at $-k_z$ with no change of chirality, thus giving rise to each independent octet of Weyl nodes in Fig. 2(a) where the S_4 symmetry maps each Weyl node at a fixed k_z to a Weyl node of opposite chirality at $-k_z$. In contrast, the symmetries of phase III require that each quartet of Weyl nodes at a fixed k_z has a unique chirality as imposed by C_{4z} symmetry, and similarly for the quartet mapped to $-k_z$ by $C_{2z}T$, thus giving rise to octets of Weyl nodes of the same chirality. While the transition from one phase to another requires the splitting of the octets into D_2-symmetric quartets of the same chirality (each contained in one of the two vertical C_2T planes), the intrinsic incompatibility between the D_{2d}-symmetric octets of alternating chirality and the D_4-symmetric octets of the same chirality enforces a qualitative rearrangement of the Weyl nodes through the Brillouin zone across the structural phase transition. It is worth noting that unlike the situation in real space where each atom can move along three independent degrees of freedom, Weyl nodes pinned on the C_2T-invariant planes in reciprocal space only have two degrees of freedom, as a single Weyl node on a given C_2T-invariant plane cannot get out of that plane unless it recombines with another Weyl node. Therefore, the Weyl nodes are forced to move a large distance across the Brillouin zone as the structural phase transition occurs, despite the very small temperature change and associated small atomic displacements in real space.

The trajectories of the Weyl nodes shown in Figs. 2(b) and 2(c) demonstrate the above scenario. In the initial configuration the Weyl nodes on the two vertical $C_{2i}T$-invariant planes ($i = x, y$) are mirror images of each other. When the system gradually approaches phase III with C_{4z} symmetry, the four "red" Weyl nodes with $|k_z| > 0$ on the $C_{2x}T$-invariant plane first move vertically on the plane and then meet their C_{2y}-symmetric partners at the k_y axis. After that, they transfer to the $C_{2z}T$-invariant plane and move toward their corresponding C_{2z}-symmetric partners until meeting at the k_x axis. Finally they leave the $C_{2z}T$-invariant plane and stop somewhere on the $C_{2y}T$-invariant plane [as indicated by the red arrows in Fig. 2(b)], forming a D_4-symmetric octet of red chirality together with another four Weyl nodes on the $C_{2x}T$-invariant plane [indicated by the red arrows in Fig. 2(c)] which are initially located on the $C_{2z}T$-invariant plane and slightly separated by the k_y axis. It is worth noting that in order to migrate from one vertical C_2T-invariant plane to another, every Weyl node indicated in Fig. 2(b) travels a quarter of the horizontal C_2T-invariant plane and moves up to 0.47 Å^{-1} in total, which is 49% of the cubic root of the volume of the Brillouin zone. Figure 2(c) shows another example of significant motion of Weyl nodes. The four Weyl nodes with "blue" chirality that are initially located on the horizontal $C_{2z}T$-invariant plane first meet at the k_x axis, then each of them shifts over an arc on the $C_{2y}T$-invariant plane and merges with its C_{2z}-symmetric partner at the intersection of the $C_{2x}T$- and $C_{2y}T$-invariant

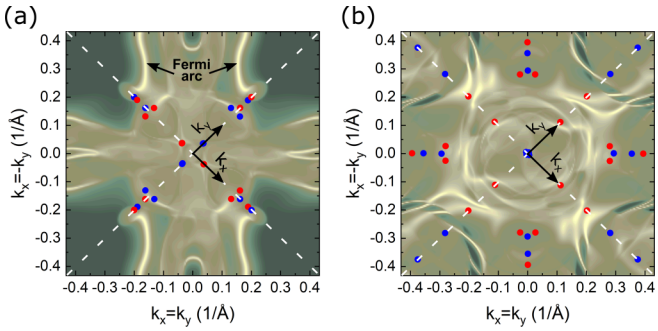

FIG. 3. $\boldsymbol{k}$-dependent local density of states (LDOS) for phases (a) II and (b) III on the [001] surface, where gold (olive) color represents high (low) LDOS. The diagonal dashed lines highlight the projections of $C_{2x}T$- and $C_{2y}T$-invariant planes on the [001] surface. The red and blue dots show the projected positions of bulk Weyl nodes on the [001] surface.

planes, which is the C_{4z} axis, with a total distance of 30% the cubic root of the volume of the Brillouin zone.

Due to the bulk-boundary correspondence, the movement of bulk Weyl nodes can also be traced in terms of the surface Fermi arcs. Figures 3(a) and 3(b) show the surface states of phases II and III on the [001] surface. We note that phase II exhibits an ideal Weyl semimetal feature: two thick and straight Fermi arcs connecting the projection of the $C_{2x}T$- and $C_{2y}T$-invariant planes, which should be easily detected by surface angle-resolved photoemission spectroscopy (ARPES). To reach the fourfold rotational symmetry in phase III, the Fermi arcs in phase II must be broken, therefore the Fermi arcs in phase III are more local and not as obvious as in phase II (see the video of the surface state evolution in the SM [71]).

C_2-indicated locking of Weyl nodes and unlocking through braiding. Crucially, we find that the long-distance movement of a subset of Weyl nodes in $Cd_2Re_2O_7$ is able to induce a novel topological phase transition between two distinct Euler classes [28,34,72]. This finding also reveals the insights that the locking of the Weyl nodes on the C_2T-invariant planes in $Cd_2Re_2O_7$ is essentially a consequence of nontrivial Euler class topology, and as a result, a non-Abelian braiding process must take place before Weyl node pairs transfer from one C_2T plane to another.

To understand better the above insights, we now call the Weyl nodes considered so far the *principal* nodes, and the node within the next energy gap below (or above), the lower (higher) *adjacent* nodes. Taking as an example the C_{2x}-symmetric pair of principal nodes located within the horizontal $C_{2z}T$-invariant plane at $k_x > 0$ whose trajectories have been indicated by the blue arrows in Fig. 2(c), let us first consider what would happen without braiding. In phase II, the bands forming the principal nodes on the ΓX line have opposite C_{2x} eigenvalues (see the band structure in the SM [73]). In the absence of braiding, the merging of the two principal nodes on the ΓX line would induce a band inversion along the C_{2x} axis between two bands of opposite C_{2x} eigenvalues, forming two unavoided band crossings on the ΓX line that are protected by C_{2x} symmetry (see also Ref. [74]). As a consequence, the two principal nodes would scatter on the ΓX line, thus remaining on the $C_{2z}T$-invariant plane after their merging. Such a scattering of Weyl node pairs confined on a C_2T-invariant plane is recognized recently to be associated with a nontrivial C_2T-Euler class topology [28]. To strictly confirm this, we have numerically computed the Euler class on a patch of the $C_{2z}T$-invariant plane that contains the two principal nodes under consideration while avoiding all other nodes (see calculation details in the SM [73], and also Refs. [28,75–78] therein), from which we obtain the Euler class $\chi_{C_{2z}T} = 1$. The nonvanishing $\chi_{C_{2z}T}$ also indicates an equal $C_{2z}T$-non-Abelian frame charge of the two principal nodes [28,32,34,70,72], which should lead to a topological obstruction to transferring them to the vertical $C_{2y}T$-invariant plane. However, we have seen in Fig. 2(c) that the movement of two principal nodes successfully overcomes this topological obstruction, which is impossible to take place if the principal nodes do not braid with the adjacent nodes below or above. Indeed, as shown in Figs. 4(a)–4(f) with successive snapshots of the band structure during the phase transition, we find that a band inversion within the lower adjacent gap occurs along the ΓX line, leading to the exchange of the C_{2x} eigenvalue of the lower band and giving rise to two lower adjacent nodes along the C_{2x} axis. We then observe that the two principal nodes merge on the ΓX line, which now involves two bands of equal C_{2x} eigenvalue. As a result, the band inversion in the principal gap along the ΓX line now induces avoided band crossings, allowing the transfer of the two principal nodes from the horizontal $C_{2z}T$-invariant plane to the vertical $C_{2y}T$-invariant plane. On top of that, the appearance of the avoided band crossing also implies that the $C_{2z}T$- and $C_{2x}T$-Euler classes on patches that avoid the adjacent nodes are now both zero. In summary, we find that the $C_{2z}T$-Euler class in phase II readily follows from the opposite nature of the C_{2x} eigenvalues of the bands forming the principal nodes. In this regard, the unlocking of the Weyl nodes from the $C_{2z}T$-invariant plane is indicated by the exchange of the C_{2x}-eigenvalue of the lower band, which is induced by the braiding through an adjacent band inversion. It is remarkable that the whole process can be experimentally probed by bulk temperature-dependent ARPES.

Generalizations. We emphasize that the physical manifestations addressed in this work are controlled by symmetry, and not by the details of the specific material involved. Other materials have also been shown to undergo a structural phase transition mediated by a Goldstone mode, such as the hexagonal manganites [79–81]. A common feature of these systems is the breaking of the $U(1)$ symmetry of their energy landscape (as an effect of the discrete point group symmetry of the crystal) with discrete minima separated by small potential barriers. While in our case this facilitates an unconventional phase transition between two isomorphic but distinct crystal structures, in the case of the hexagonal manganites, the high-temperature phase $P6_3/mmc$ (D_{6h}) gives rise to two non-isomorphic low-temperature phases $P6_3cm$ (C_{6v}) and $P\bar{3}c1$ (D_{3d}), both of which exhibit a sixfold degenerate ground state. Focusing on the noncentrosymmetric phase ($P6_3cm$) which is the only one permitting Weyl nodes from a symmetry perspective, each discrete minimum corresponds to a distinct polar lattice distortion (combining three Mn trimerizations and two ferroelectric polarizations) [79,80,82,83]. This suggests that our framework would also apply in the case of a transition between two distinct polar phases. These questions, as well

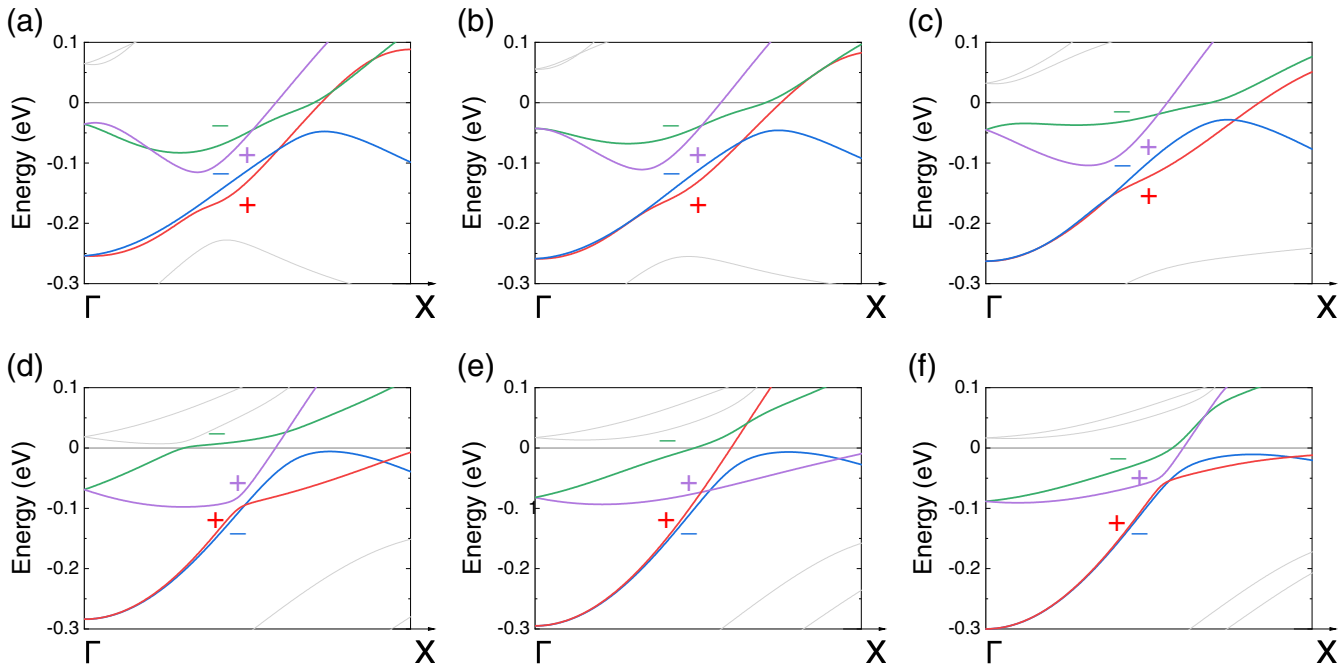

FIG. 4. (a)–(f) Snapshots of the band structure along the ΓX line during the structural phase transition. The "+" sign and "−" sign mark the C_{2x} eigenvalues of the bands with the same color as the symbol.

as studies into other symmetry groups and materials, provide intriguing future research directions.

Conclusions and discussion. In conclusion, we have shown that the structural phase transition in the materials science sense can result in relatively large movements of Weyl nodes due to symmetry changes across the transition. The transition also involves multiple interesting braiding processes of Weyl nodes which then leads to a change in Euler invariant and thus a phase transition in the topological sense. In addition, the transition offers an interesting route to significantly move Weyl nodes and their associated Fermi arcs using only moderate temperature changes. Although the principles behind the mechanism are generic, we have also discussed a specific material example in the form of $Cd_2Re_2O_7$. We note a recent high-throughput screening for Weyl semimetals with fourfold rotoinversion symmetry [84], and based on our findings it is worthwhile to explore whether these candidates may have any phase transition from S_4 to C_4, which would suggest similar physics to that reported here.

Acknowledgments. S.C. acknowledges financial support from the Cambridge Trust and from the Winton Programme for the Physics of Sustainability. R.-J.S. acknowledges funding from the Marie Skłodowska-Curie Programme under EC Grant No. 842901, the Winton Programme for the Physics of Sustainability, and Trinity College at the University of Cambridge. B.M. acknowledges support from a UKRI Future Leaders Fellowship (Grant No. MR/V023926/1), from the Gianna Angelopoulos Programme for Science, Technology, and Innovation, and from the Winton Programme for the Physics of Sustainability. The calculations in this work have been performed using resources provided by the Cambridge Tier-2 system [operated by the University of Cambridge Research Computing Service and funded by EPSRC (Grant No. EP/P020259/1)], as well as by the UK Materials and Molecular Modelling Hub [partially funded by EPSRC (Grant No. EP/P020194)], Thomas, and by the UK National Supercomputing Service, ARCHER. Access to Thomas and ARCHER was obtained via the UKCP consortium and funded by EPSRC Grant No. EP/P022561/1.

[1] X.-L. Qi and S.-C. Zhang, Topological insulators and superconductors, Rev. Mod. Phys. **83**, 1057 (2011).

[2] M. Z. Hasan and C. L. Kane, *Colloquium*: Topological insulators, Rev. Mod. Phys. **82**, 3045 (2010).

[3] L. Fu, Topological Crystalline Insulators, Phys. Rev. Lett. **106**, 106802 (2011).

[4] R.-J. Slager, A. Mesaros, V. Juričić, and J. Zaanen, The space group classification of topological band-insulators, Nat. Phys. **9**, 98 (2013).

[5] J. Kruthoff, J. de Boer, J. van Wezel, C. L. Kane, and R.-J. Slager, Topological Classification of Crystalline Insulators through Band Structure Combinatorics, Phys. Rev. X **7**, 041069 (2017).

[6] A. Bouhon and A. M. Black-Schaffer, Global band topology of simple and double Dirac-point semimetals, Phys. Rev. B **95**, 241101(R) (2017).

[7] H. C. Po, A. Vishwanath, and H. Watanabe, Symmetry-based indicators of band topology in the 230 space groups, Nat. Commun. **8**, 50 (2017).

[8] B. Bradlyn, L. Elcoro, J. Cano, M. G. Vergniory, Z. Wang, C. Felser, M. I. Aroyo, and B. A. Bernevig, Topological quantum chemistry, Nature (London) **547**, 298 (2017).

[9] R.-J. Slager, The translational side of topological band insulators, J. Phys. Chem. Solids **128**, 24 (2019).

[10] J. Höller and A. Alexandradinata, Topological Bloch oscillations, Phys. Rev. B **98**, 024310 (2018).

[11] V. Juričić, A. Mesaros, R.-J. Slager, and J. Zaanen, Universal Probes of Two-Dimensional Topological Insulators: Dislocation and π flux, Phys. Rev. Lett. **108**, 106403 (2012).

[12] M. S. Scheurer and R.-J. Slager, Unsupervised Machine Learning and Band Topology, Phys. Rev. Lett. **124**, 226401 (2020).

[13] R.-J. Slager, A. Mesaros, V. Juričić, and J. Zaanen, Interplay between electronic topology and crystal symmetry: Dislocation-line modes in topological band insulators, Phys. Rev. B **90**, 241403(R) (2014).

[14] K. Shiozaki, M. Sato, and K. Gomi, Topological crystalline materials: General formulation, module structure, and wallpaper groups, Phys. Rev. B **95**, 235425 (2017).

[15] C. Fang, M. J. Gilbert, and B. A. Bernevig, Bulk topological invariants in noninteracting point group symmetric insulators, Phys. Rev. B **86**, 115112 (2012).

[16] H. Watanabe, H. C. Po, and A. Vishwanath, Structure and topology of band structures in the 1651 magnetic space groups, Sci. Adv. **4** (2018).

[17] L. Elcoro, B. J. Wieder, Z. Song, Y. Xu, B. Bradlyn, and B. A. Bernevig, Magnetic topological quantum chemistry, Nat. Commun. **12**, 5965 (2021).

[18] A. Bouhon, G. F. Lange, and R.-J. Slager, Topological correspondence between magnetic space group representations and subdimensions, Phys. Rev. B **103**, 245127 (2021).

[19] B. J. Wieder, Y. Kim, A. M. Rappe, and C. L. Kane, Double Dirac Semimetals in Three Dimensions, Phys. Rev. Lett. **116**, 186402 (2016).

[20] G. F. Lange, A. Bouhon, and R.-J. Slager, Subdimensional topologies, indicators, and higher order boundary effects, Phys. Rev. B **103**, 195145 (2021).

[21] H. C. Po, H. Watanabe, and A. Vishwanath, Fragile Topology and Wannier Obstructions, Phys. Rev. Lett. **121**, 126402 (2018).

[22] B. J. Wieder and B. A. Bernevig, The axion insulator as a pump of fragile topology, arXiv:1810.02373.

[23] A. Bouhon, A. M. Black-Schaffer, and R.-J. Slager, Wilson loop approach to fragile topology of split elementary band representations and topological crystalline insulators with time-reversal symmetry, Phys. Rev. B **100**, 195135 (2019).

[24] N. P. Armitage, E. J. Mele, and A. Vishwanath, Weyl and Dirac semimetals in three-dimensional solids, Rev. Mod. Phys. **90**, 015001 (2018).

[25] S. Kobayashi and M. Sato, Topological Superconductivity in Dirac Semimetals, Phys. Rev. Lett. **115**, 187001 (2015).

[26] M. Sato and S. Fujimoto, Topological phases of noncentrosymmetric superconductors: Edge states, majorana fermions, and non-Abelian statistics, Phys. Rev. B **79**, 094504 (2009).

[27] J. Ahn, S. Park, and B.-J. Yang, Failure of Nielsen-Ninomiya Theorem and Fragile Topology in Two-Dimensional Systems with Space-Time Inversion Symmetry: Application to Twisted Bilayer Graphene at Magic Angle, Phys. Rev. X **9**, 021013 (2019).

[28] A. Bouhon, QuanSheng Wu, R.-J. Slager, H. Weng, O. V. Yazyev, and T. Bzdušek, Non-Abelian reciprocal braiding of Weyl points and its manifestation in ZrTe, Nat. Phys. **16**, 1137 (2020).

[29] G. F. Lange, A. Bouhon, B. Monserrat, and R.-J. Slager, Topological continuum charges of acoustic phonons in two dimensions and the Nambu-Goldstone theorem, Phys. Rev. B **105**, 064301 (2022).

[30] B. Peng, A. Bouhon, R.-J. Slager, and B. Monserrat, Multigap topology and non-Abelian braiding of phonons from first principles, Phys. Rev. B **105**, 085115 (2022).

[31] A. J. Beekman, J. Nissinen, K. Wu, K. Liu, R.-J. Slager, Z. Nussinov, V. Cvetkovic, and J. Zaanen, Dual gauge field theory of quantum liquid crystals in two dimensions, Phys. Rep. **683**, 1 (2017).

[32] QuanSheng Wu, A. A. Soluyanov, and T. Bzdušek, Non-Abelian band topology in noninteracting metals, Science **365**, 1273 (2019).

[33] V. Könye, A. Bouhon, I. C. Fulga, R.-J. Slager, J. van den Brink, and J. I. Facio, Chirality flip of Weyl nodes and its manifestation in strained $mote_2$, Phys. Rev. Research **3**, L042017 (2021).

[34] A. Bouhon, T. Bzdušek, and R.-J. Slager, Geometric approach to fragile topology beyond symmetry indicators, Phys. Rev. B **102**, 115135 (2020).

[35] B. Peng, A. Bouhon, B. Monserrat, and R.-J. Slager, Phonons as a platform for non-Abelian braiding and its manifestation in layered silicates, Nat. Commun. **13**, 423 (2022).

[36] B. Jiang, A. Bouhon, Z.-K. Lin, X. Zhou, B. Hou, F. Li, R.-J. Slager, and J.-H. Jiang, Experimental observation of non-Abelian topological acoustic semimetals and their phase transitions, Nat. Phys. **17**, 1239 (2021).

[37] F. N. Ünal, A. Bouhon, and R.-J. Slager, Topological Euler Class as a Dynamical Observable in Optical Lattices, Phys. Rev. Lett. **125**, 053601 (2020).

[38] R. Ilan, A. G. Grushin, and D. I. Pikulin, Pseudo-electromagnetic fields in 3D topological semimetals, Nat. Rev. Phys. **2**, 29 (2020).

[39] E. J. Sie, C. M. Nyby, C. D. Pemmaraju, S. J. Park, X. Shen, J. Yang, M. C. Hoffmann, B. K. Ofori-Okai, R. Li, A. H. Reid *et al.*, An ultrafast symmetry switch in a Weyl semimetal, Nature (London) **565**, 61 (2019).

[40] R.-J. Slager, V. Juričić, V. Lahtinen, and J. Zaanen, Self-organized pseudo-graphene on grain boundaries in topological band insulators, Phys. Rev. B **93**, 245406 (2016).

[41] C. L. Zhang, S. Y. Xu, C. M. Wang, Z. Lin, Z. Z. Du, C. Guo, C. C. Lee, H. Lu, Y. Feng, S. M. Huang *et al.*, Magnetic-tunnelling-induced Weyl node annihilation in TaP, Nat. Phys. **13**, 979 (2017).

[42] F. de Juan, A. G. Grushin, T. Morimoto, and J. E. Moore, Quantized circular photogalvanic effect in Weyl semimetals, Nat. Commun. **8**, 15995 (2017).

[43] J. H. Pixley, D. A. Huse, and S. D. Sarma, Rare-Region-Induced Avoided Quantum Criticality in Disordered Three-Dimensional Dirac and Weyl Semimetals, Phys. Rev. X **6**, 021042 (2016).

[44] R.-J. Slager, V. Juričić, and B. Roy, Dissolution of topological Fermi arcs in a dirty Weyl semimetal, Phys. Rev. B **96**, 201401(R) (2017).

[45] J. H. Pixley and J. H. Wilson, Rare regions and avoided quantum criticality in disordered Weyl semimetals and superconductors, Ann. Phys. **435**, 168455 (2021).

[46] B. Roy, R.-J. Slager, and V. Juričić, Global Phase Diagram of a Dirty Weyl Liquid and Emergent Superuniversality, Phys. Rev. X **8**, 031076 (2018).

[47] R. Jin, J. He, S. McCall, C. S. Alexander, F. Drymiotis, and D. Mandrus, Superconductivity in the correlated pyrochlore $Cd_2Re_2O_7$, Phys. Rev. B **64**, 180503(R) (2001).

[48] H. Sakai, K. Yoshimura, H. Ohno, H. Kato, S. Kambe, R. E. Walstedt, T. D. Matsuda, Y. Haga, and Y. Onuki, Superconductivity in a pyrochlore oxide, $Cd_2Re_2O_7$, J. Phys.: Condens. Matter **13**, L785 (2001).

[49] Jun-ichi Yamaura, K. Takeda, Y. Ikeda, N. Hirao, Y. Ohishi, T. C. Kobayashi, and Z. Hiroi, Successive spatial symmetry breaking under high pressure in the spin-orbit-coupled metal $Cd_2Re_2O_7$, Phys. Rev. B **95**, 020102(R) (2017).

[50] P. C. Donohue, J. M. Longo, R. D. Rosenstein, and L. Katz, The preparation and structure of cadmium rhenium oxide, $Cd_2Re_2O_7$, Inorg. Chem. **4**, 1152 (1965).

[51] M. Hanawa, Y. Muraoka, T. Tayama, T. Sakakibara, J. Yamaura, and Z. Hiroi, Superconductivity at 1 K in $Cd_2Re_2O_7$, Phys. Rev. Lett. **87**, 187001 (2001).

[52] J. P. Castellan, B. D. Gaulin, J. van Duijn, M. J. Lewis, M. D. Lumsden, R. Jin, J. He, S. E. Nagler, and D. Mandrus, Structural ordering and symmetry breaking in $Cd_2Re_2O_7$, Phys. Rev. B **66**, 134528 (2002).

[53] J.-I. Yamaura and Z. Hiroi, Low temperature symmetry of pyrochlore oxide $Cd_2Re_2O_7$, J. Phys. Soc. Jpn. **71**, 2598 (2002).

[54] Z. Hiroi, J.-I. Yamaura, Y. Muraoka, and M. Hanawa, Second phase transition in pyrochlore oxide $Cd_2Re_2O_7$, J. Phys. Soc. Jpn. **71**, 1634 (2002).

[55] S. Uji, H. T. Hirose, T. Terashima, Y. Matsubayashi, D. Hirai, Z. Hiroi, and T. Hasegawa, Successive continuous phase transitions in spin-orbit coupled metal $Cd_2Re_2O_7$, J. Phys. Soc. Jpn. **90**, 064714 (2021).

[56] Y. Matsubayashi, K. Sugii, D. Hirai, Z. Hiroi, T. Hasegawa, S. Sugiura, H. T. Hirose, T. Terashima, and S. Uji, Coexistence of odd-parity and even-parity order parameters in the multipole order phase of the spin-orbit coupled metal $Cd_2Re_2O_7$, Phys. Rev. B **101**, 205133 (2020).

[57] J. P. Perdew, A. Ruzsinszky, G. I. Csonka, O. A. Vydrov, G. E. Scuseria, L. A. Constantin, X. Zhou, and K. Burke, Restoring the Density-Gradient Expansion for Exchange in Solids and Surfaces, Phys. Rev. Lett. **100**, 136406 (2008).

[58] M. Hellenbrandt, The inorganic crystal structure database (ICSD)—Present and future, Cryst. Rev. **10**, 17 (2004).

[59] See Sec. I of the Supplemental Material at http://link.aps.org/supplemental/10.1103/PhysRevB.105.L081117 for the details of the first-principle calculations and the phonon dispersion of phase I.

[60] G. Kresse and J. Furthmüller, Efficient iterative schemes for *ab initio* total-energy calculations using a plane-wave basis set, Phys. Rev. B **54**, 11169 (1996).

[61] G. Kresse and J. Furthmüller, Efficiency of ab-initio total energy calculations for metals and semiconductors using a plane-wave basis set, Comput. Mater. Sci. **6**, 15 (1996).

[62] J. H. Lloyd-Williams and B. Monserrat, Lattice dynamics and electron-phonon coupling calculations using nondiagonal supercells, Phys. Rev. B **92**, 184301 (2015).

[63] S. Chen, R. Maezono, J. Chen, F. M. Grosche, C. J. Pickard, and B. Monserrat, Chemical and structural stability of superconducting In_5Bi_3 driven by spin–orbit coupling, J. Phys.: Mater. **3**, 015007 (2019).

[64] G. Henkelman and H. Jónsson, Improved tangent estimate in the nudged elastic band method for finding minimum energy paths and saddle points, J. Chem. Phys. **113**, 9978 (2000).

[65] L. Fu, Parity-Breaking Phases of Spin-Orbit-Coupled Metals with Gyrotropic, Ferroelectric, and Multipolar Orders, Phys. Rev. Lett. **115**, 026401 (2015).

[66] I. A. Sergienko and S. H. Curnoe, Structural order parameter in the pyrochlore superconductor $Cd_2Re_2O_7$, J. Phys. Soc. Jpn. **72**, 1607 (2003).

[67] C. A. Kendziora, I. A. Sergienko, R. Jin, J. He, V. Keppens, B. C. Sales, and D. Mandrus, Goldstone-Mode Phonon Dynamics in the Pyrochlore $Cd_2Re_2O_7$, Phys. Rev. Lett. **95**, 125503 (2005).

[68] J. Venderley, M. Matty, K. Mallayya, M. Krogstad, J. Ruff, G. Pleiss, V. Kishore, D. Mandrus, D. Phelan, L. Poudel *et al.*, Harnessing interpretable and unsupervised machine learning to address big data from modern x-ray diffraction, arXiv:2008.03275.

[69] O. Vyaselev, K. Kobayashi, K. Arai, J. Yamazaki, K. Kodama, M. Takigawa, M. Hanawa, and Z. Hiroi, Cd and Re NMR/NQR in pyrochlore compound $Cd_2Re_2O_7$, in *Proceedings of the 8th ISSP International Symposium*, J. Phys. Chem. Solids **63**, 1031 (2002).

[70] X.-Q. Sun, S.-C. Zhang, and T. Bzdušek, Conversion Rules for Weyl Points and Nodal Lines in Topological Media, Phys. Rev. Lett. **121**, 106402 (2018).

[71] See Supplemental Material at http://link.aps.org/supplemental/10.1103/PhysRevB.105.L081117 for the video showing the evolution of the surface state on the [001] surface during the phase transition from phase II to phase III.

[72] J. Ahn and B.-J. Yang, Symmetry representation approach to topological invariants in $C_{2z}t$-symmetric systems, Phys. Rev. B **99**, 235125 (2019).

[73] See Sec. II of the Supplemental Material at http://link.aps.org/supplemental/10.1103/PhysRevB.105.L081117 for the band structure of phase II along the high-symmetry path. See Sec. III for the technical details of the calculation of the Euler class.

[74] S. Murakami, M. Hirayama, R. Okugawa, and T. Miyake, Emergence of topological semimetals in gap closing in semiconductors without inversion symmetry, Sci. Adv. **3**, e1602680 (2017).

[75] A. A. Mostofi, J. R. Yates, G. Pizzi, Y.-S. Lee, I. Souza, D. Vanderbilt, and N. Marzari, An updated version of wannier90: A tool for obtaining maximally-localised Wannier functions, Comput. Phys. Commun. **185**, 2309 (2014).

[76] D. Gresch, QuanSheng Wu, G. W. Winkler, R. Häuselmann, M. Troyer, and A. A. Soluyanov, Automated construction of symmetrized Wannier-like tight-binding models from *ab initio* calculations, Phys. Rev. Materials **2**, 103805 (2018).

[77] T. Bzdušek, Euler class of a pair of energy bands on a manifold with a boundary, ResearchGate (2019), publicly available *Mathematica* code.

[78] A. M. Chebotarev and A. E. Teretenkov, Singular value decomposition for the Takagi factorization of symmetric matrices, Appl. Math. Comput. **234**, 380 (2014).

[79] S. H. Skjærvø, Q. N. Meier, M. Feygenson, N. A. Spaldin, S. J. L. Billinge, E. S. Bozin, and S. M. Selbach, Unconventional Continuous Structural Disorder at the Order-Disorder Phase Transition in the Hexagonal Manganites, Phys. Rev. X **9**, 031001 (2019).

[80] Q. N. Meier, A. Stucky, J. Teyssier, S. M. Griffin, D. van der Marel, and N. A. Spaldin, Manifestation of structural Higgs and Goldstone modes in the hexagonal manganites, Phys. Rev. B **102**, 014102 (2020).

[81] D. M. Juraschek, Q. N. Meier, and P. Narang, Parametric Excitation of an Optically Silent Goldstone-Like Phonon Mode, Phys. Rev. Lett. **124**, 117401 (2020).

[82] F.-T. Huang, X. Wang, S. M. Griffin, Y. Kumagai, O. Gindele, M.-W. Chu, Y. Horibe, N. A. Spaldin, and S.-W. Cheong, Duality of Topological Defects in Hexagonal Manganites, Phys. Rev. Lett. **113**, 267602 (2014).

[83] Y. Kumagai, A. A. Belik, M. Lilienblum, N. Leo, M. Fiebig, and N. A. Spaldin, Observation of persistent centrosymmetricity in the hexagonal manganite family, Phys. Rev. B **85**, 174422 (2012).

[84] J. Gao, Y. Qian, S. Nie, Z. Fang, H. Weng, and Z. Wang, High-throughput screening for Weyl semimetals with S4 symmetry, Sci. Bull. **66**, 667 (2021).